Supplementary Information (SI) for Nanoscale.
This journal is © The Royal Society of Chemistry 2025

Supporting Information

Broadband and omnidirectional antireflective film with bioinspired nanocone-grid hybrid structures for enhanced solar energy harvesting

Zhibin Jiao,[a] Shuhan Zhang,[a] Chuanhao Zhao,[a] Xueyang Li,[b] Zhaozhi Wang,[a] Jing Zhao,[a] Hanliang Ding,*[b] Bo Li,*[bc] Shichao Niu,[bc] and Zhiwu Han[bc]

[a] School of Mechanical Engineering, Shenyang University of Technology, Shenyang 110870, China.

[b] Key Laboratory of Bionic Engineering (Ministry of Education), Jilin University, Changchun 130022, China.

[c] Institute of Structured and Architected Materials, Liaoning Academy of Materials, Shenyang 110167, China

To further characterize the primary composition of the dragonfly wing material, the Fourier transform infrared (FTIR) spectroscopy was employed to identify the functional groups on the wing surface, with the corresponding spectrum presented in Fig. S1. Below is the detailed assignment of characteristic peaks and their associated molecular structures. A broad absorption peak centered at 3295 cm^{-1} is attributed to the overlapping stretching vibrations of O–H and N–H bonds, which is consistent with the superimposed absorption features of hydroxyl (–OH) and acetamido ($–NHCOCH_3$) groups in chitin molecules. The broadening of this peak indicates the formation of an intermolecular hydrogen-bonding network, a structural characteristic typical of crystalline chitin. The peaks at 2919 cm^{-1} and 2851 cm^{-1} correspond to the asymmetric and symmetric stretching vibrations of CH_2 and CH_3 groups, respectively. These signals reflect the vibrational modes of methylene groups in the pyranose ring and acetyl side chains of chitin, providing evidence for the presence of alkyl substituents in the polysaccharide skeleton. The peak at 1645 cm^{-1}, designated as the Amide I band, arises from the coupled vibrations of C=O stretching (amide carbonyl) and N–H in-plane bending. This constitutes a diagnostic absorption feature of the acetamido group in chitin, serving as a key marker for the presence of amide moieties. Complementarily, the peak at 1536 cm^{-1} (Amide II band) results from the combination of N–H in-plane bending and C–N stretching vibrations. This further confirms the existence of acetamido groups, reinforcing the amide-containing nature of the wing material. Peaks observed at 1449 cm^{-1} and 1378 cm^{-1} are associated with CH_2/CH_3 bending and C–O–H in-plane bending vibrations, respectively. These signals reflect the conformational characteristics of the sugar ring backbone and the hydroxyl substituents attached to the pyranose structure. The peak at 1237 cm^{-1} (Amide III band) corresponds to C–N stretching and N–H out-of-plane bending vibrations, which are closely related to the intermolecular hydrogen-bonding interactions that stabilize the crystalline structure of chitin. A prominent peak at 1076 cm^{-1} is assigned to the C–O–C stretching vibration of the pyranose ring, representing the typical absorption of β-(1→4) glycosidic linkages—the fundamental structural motif of the chitin backbone.

Collectively, the FTIR spectrum of the *Orthetrum triangulare* wing exhibits high congruence with standard chitin spectral databases. The coexistence of characteristic amide bands (Amide I–III) and polysaccharide skeleton absorptions effectively rules out the presence of cellulose (devoid of amide groups) or chitosan (lacking amide bands due to deacetylation). These results confirm that the main component of the wing sample is α-chitin, whose molecular structure consists of β-(1→4)-linked N-acetylglucosamine repeating units assembled into an ordered crystalline structure via intermolecular hydrogen bonds—consistent with the biomaterial properties of arthropod exoskeletons. Notably, chitin has a reported refractive index of 1.56,[15,57] which is relatively close to that of air (n = 1.00). This moderate refractive index difference facilitates the dragonfly wing's ability to modulate Fresnel reflection induced by abrupt refractive index changes at the air-wing interface.

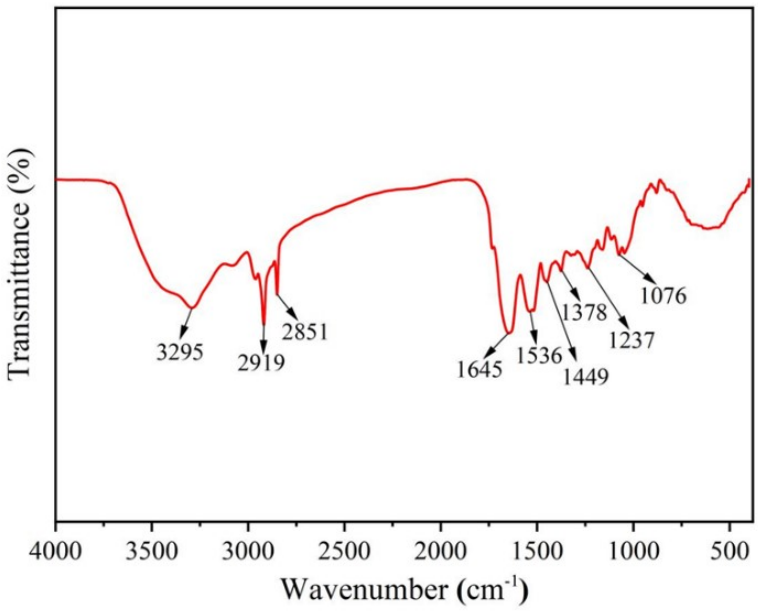

Fig. S1 FTIR spectral analysis of the wings of *Orthetrum triangulare*

Supplementary Materials I

To validate this mechanism, we constructed two models: an isolated nanocone array and a hybrid NCGL array. Both models share identical conical units (periodicity L=0.37), while the latter incorporates an additional nanograting structure (height h_2=0.5). By defining the center of the conical base as the origin of the Cartesian coordinate system, the nanocone unit can be mathematically represented as a surface of revolution generated by rotating a predefined curve about the z-axis:

$$Z = \mathrm{h}\left[1-\left(R/\mathrm{r_d}\right)^2\right] \tag{1}$$

In the formulation, where h denotes the height of the unit nanocone (1) and r_d represents its base radius (0.167), the volume of the unit nano-cone (A_1=0.0436) can be calculated. The grating unit, modeled as a truncated pyramid with trapezoidal cross-section of thickness B=0.074, yields a volume A_2=0.001. Since the NCGL structure integrates one nanocone unit with four surrounding grating units, its total volume (A_3=0.0476) is derived as $A_3 = A_1 + 4A_2$. Following Equation (1), the NCGL unit can be equivalently described as a nanocone with base radius r_e =0.176 and height h=1, generated by rotating its defining contour about the z-axis. The substrate surface is tessellated into hexagonal cells with center-to-center spacing D=0.352, each circumscribed by a circle of radius r_e. This geometric framework enables calculation of the fill factors f_1 and f_2 for the pure nano-cone array and NCGL array models, respectively, through:

$$f_1 = \frac{2\Pi \mathrm{r}_d^2}{\sqrt{3}D^2}\left(1-Z/h\right) \tag{2}$$

$$f_2 = \frac{2\Pi \mathrm{r}_\mathrm{e}^2}{\sqrt{3}D^2}\left(1-Z/h\right) \tag{3}$$

obtained $f_1 = \frac{\mathrm{r}_d^2}{\mathrm{r}_\mathrm{e}^2} f_2 \approx 0.9 f_2$

Supplementary Materials II

Based on the quantitative calculations presented in Fig. 2c, we have derived precise linear relationships between the effective refractive index n and the filling fraction f (ranging from 0 to 1) for both the nanocone structure and the NCGL graded structure:

$$n_{cone}(f) = 1.00 + 0.50f \tag{4}$$

$$n_{NCGL}(f) = 1.00 + 0.56f \tag{5}$$

These relationships clearly demonstrate that the effective refractive index can be precisely controlled by adjusting the filling fraction. In the design of the graded refractive index profile, a linear increase of the filling fraction f along the structural height h (from 0 to the total thickness L) enables a linear gradient in the refractive index for the nanocone and NCGL structures, as described by:

$$n_{cone}(h) = 1.00 + 0.50(\frac{h}{L}) \tag{6}$$

$$n_{NCGL}(h) = 1.00 + 0.56(\frac{h}{L}) \tag{7}$$

The corresponding refractive index gradients for the two structures are $0.50/L$ and $0.56/L$, respectively. Quantitative analysis confirms that the NCGL structure exhibits a broader range of refractive index modulation and a steeper gradient, providing a theoretical foundation for its superior optical performance. These quantitative results allow for the accurate and predictable design of graded refractive index profiles.

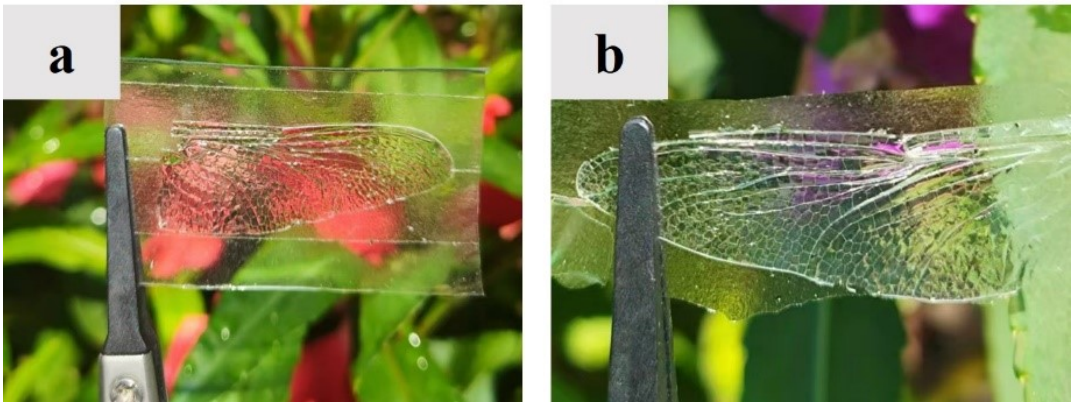

Fig. S2 The inverse-structured PDMS master and the biomimetic BOAR NOA61 film. (a) Image of the inverse-structured PDMS film; (b) Image of the biomimetic NOA61 film.

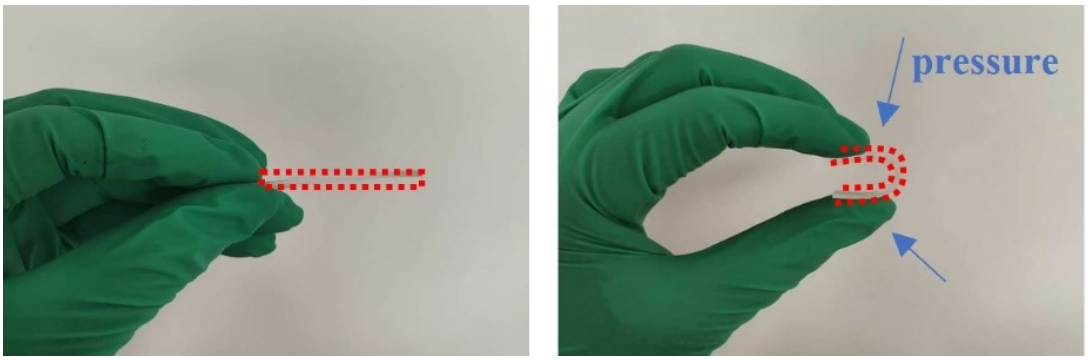

Fig. S3 Flexibility of the film, capable of being bent almost 180°.

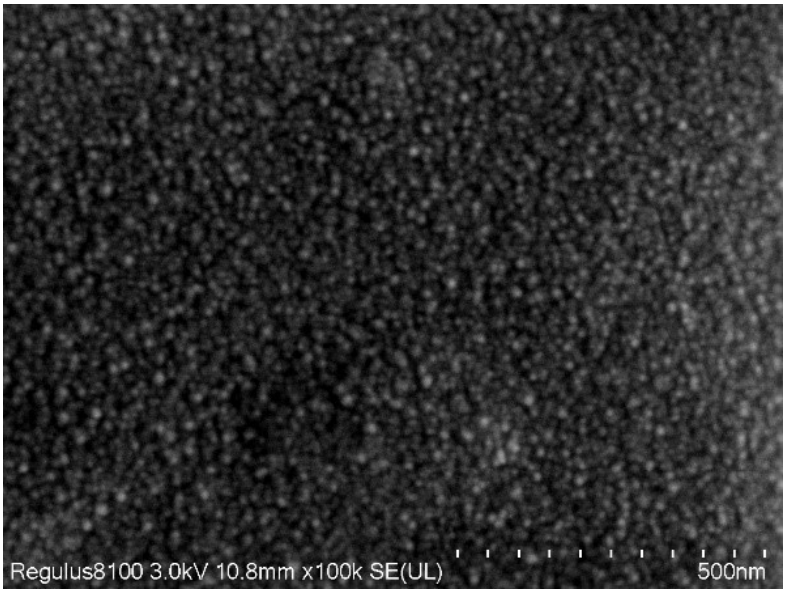

Fig. S4 SEM image of the inverse-structured PDMS film.

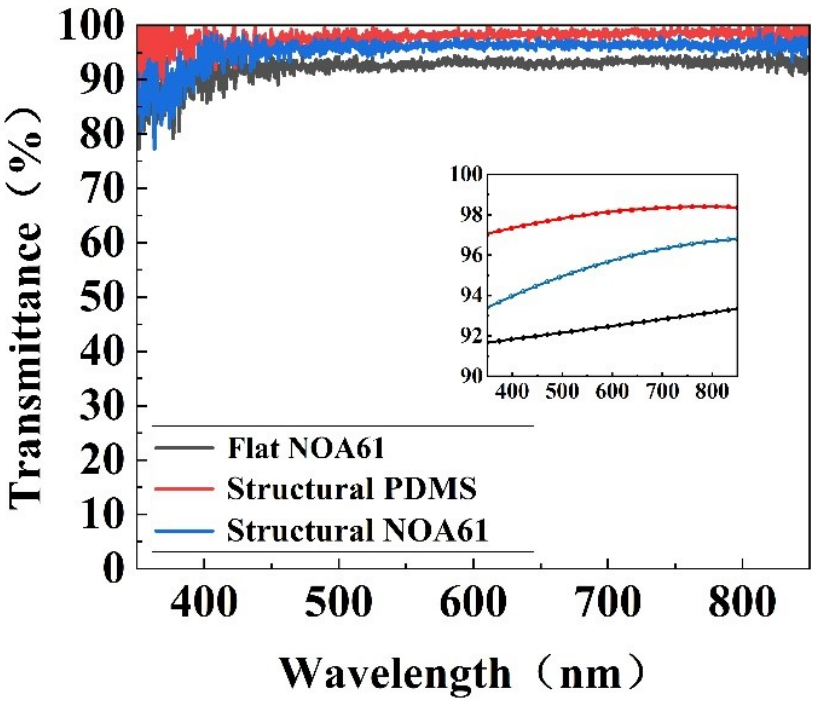

Fig. S5 Transmittance spectrum of the structured film compared to the unstructured film in the wavelength range of 350–850 nm.

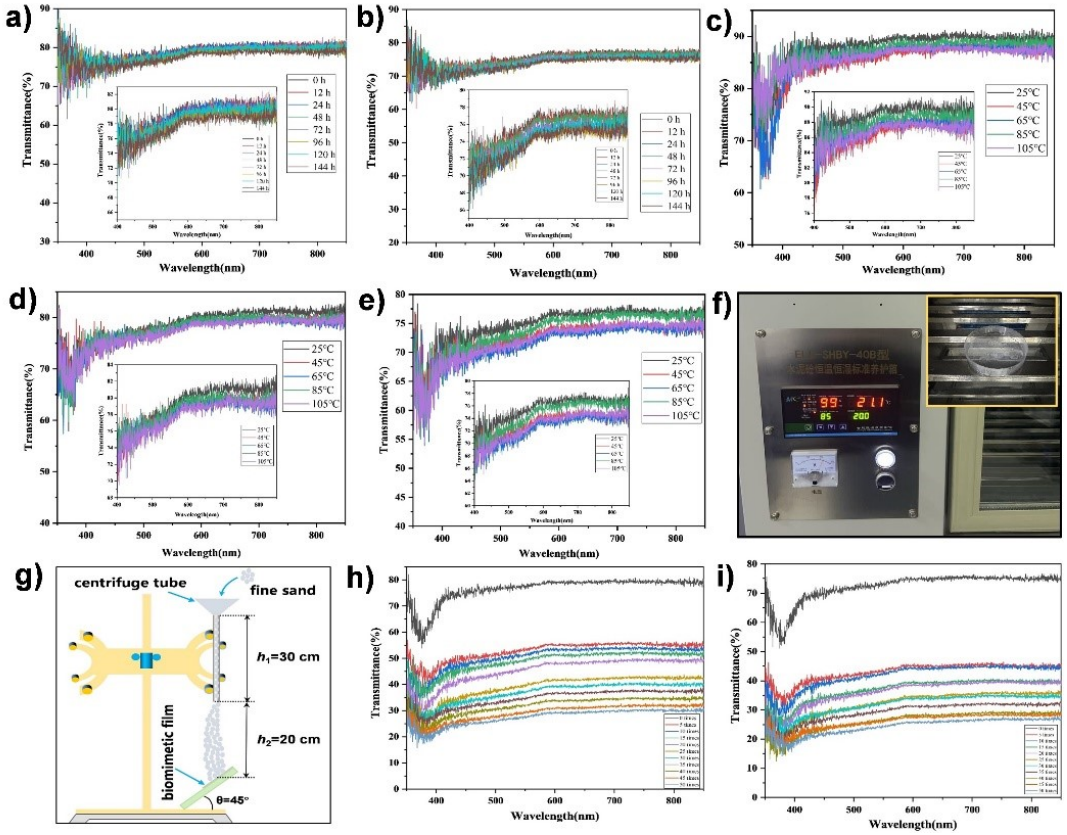

Fig. S6 Transmittance curves of the biomimetic NOA61 film after 144 hours of UV irradiation under (a) 60°and (b) 75° incidence. Transmittance curves of the film at different temperatures under (c) 30°, (d) 60°, and (e) 75° incidence. (f) Test diagram of the film's moisture retention process in a constant-humidity chamber (99% relative humidity, 20°C). (g) Schematic diagram of the sand impact test setup. Transmittance variation curves of the biomimetic NOA61 film after the sand impact test under (h) 60°and (i) 75° incidence.

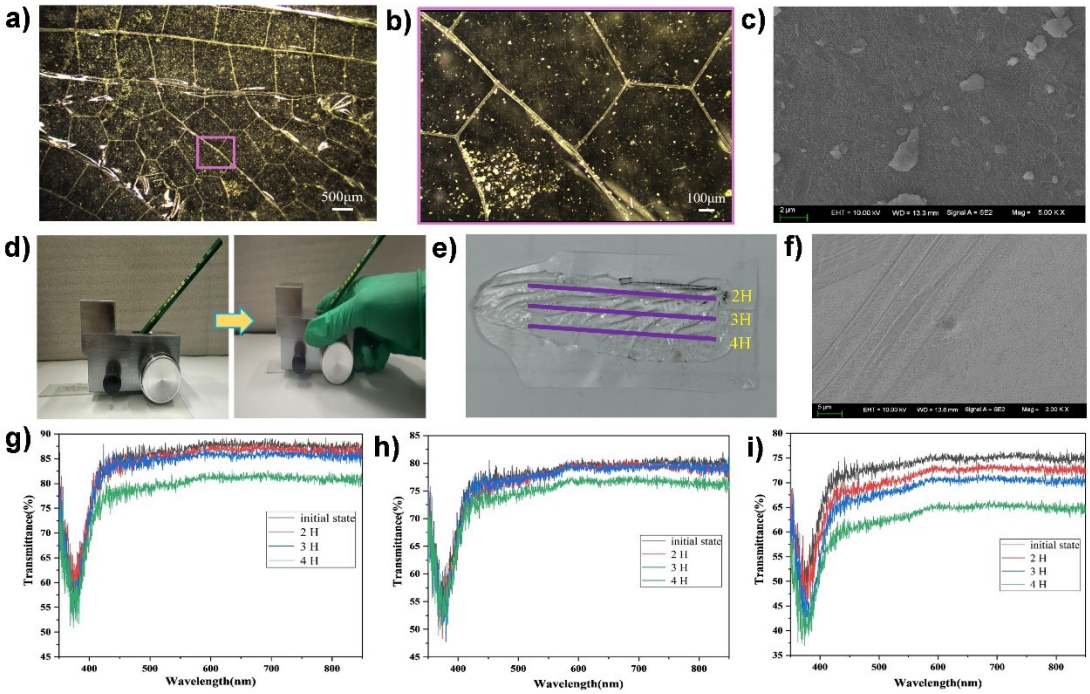

Fig. S7 (a) Ultra-depth-of-field topography image of the biomimetic surface after 50 sand impacts. (b) Magnified local topography image of the marked area in Fig. S7a. (c) SEM microtopography of the NCGL structure on the film surface after 50 sand impacts. (d) Experimental diagram of the pencil hardness test. (e) Scratch test positions of pencils with different hardness (2H/3H/4H) on the film surface. (f) SEM image of the NCGL structure damage after the 3H pencil test. Transmittance variation curves of the film after the pencil scratch test under (g) 30°, (h) 60°, and (i) 75° incidence.

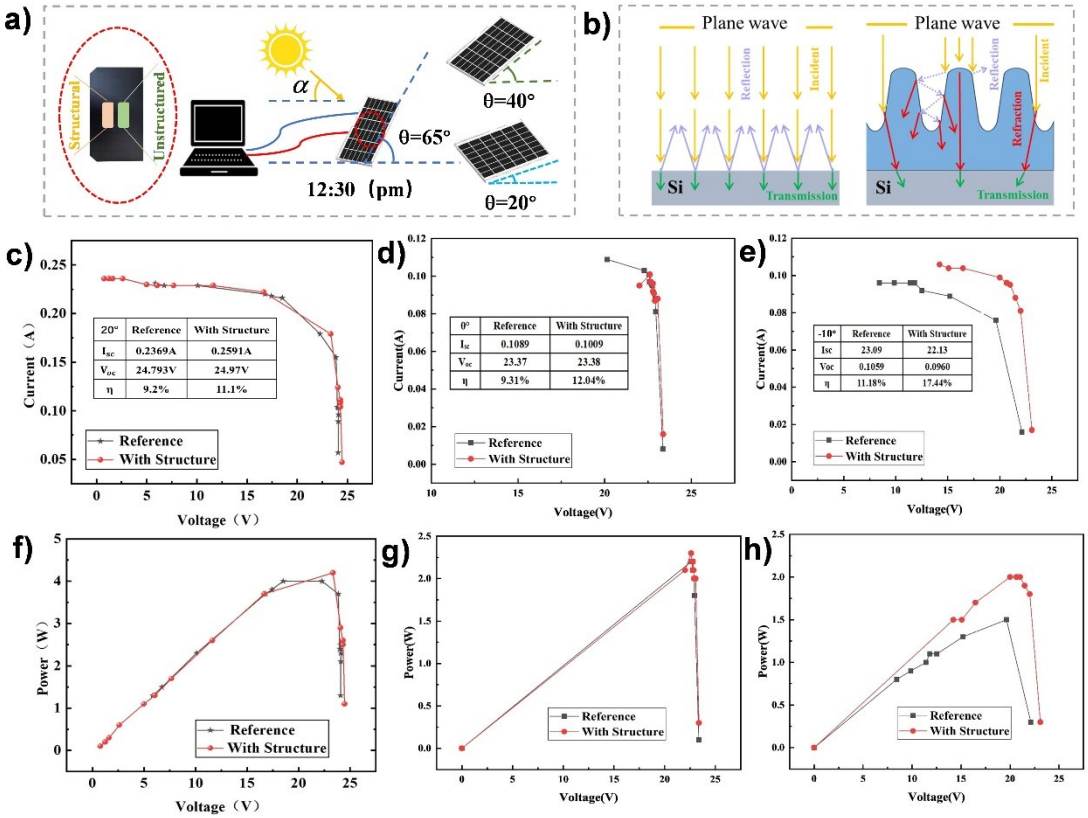

Fig. S8 Photovoltaic conversion performance of solar panels coated with biomimetic BOAR film. a) Schematic diagram of the self-built system used to test the light capture efficiency of BOAR thin-film silicon solar cells. b) Mechanism of light transmission in silicon solar cell devices. I-V characteristics of silicon solar cells coated with NCGL-structured film and unstructured film under an illumination angle of c) 45°, d) 65° and e) 75°. P-V curves of silicon solar cells with NCGL-structured film and unstructured film at an illumination angle of f) 45°, g) 65° and h) 75°.

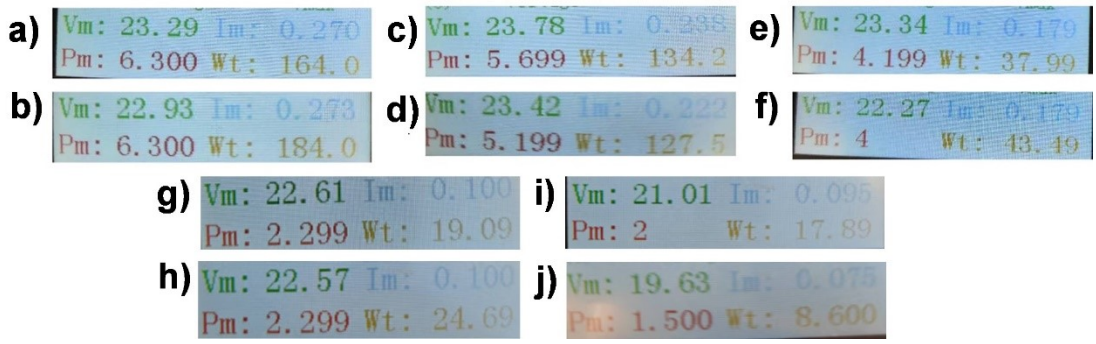

Fig. S9 Angular-dependent performance evaluation of photovoltaic panels. Power output comparison between NCGL-structured (a) and non-structured (b) thin-film solar cells at a tilt angle of 65°. (c,d), (e,f), (g,h), (i,j) show the corresponding data at tilt angles of 40°, 20°, 0°, and -10°, respectively.